Effect of surface segregation on the oxidation resistance of $Cu_3Pt(100)$

Chaoran Li,[1] Yaguang Zhu,[1] Dongxiang Wu,[1] Jorge Anibal Boscoboinik,[2] and Guangwen Zhou[1,*]

[1]*Department of Mechanical Engineering and Materials Science and Engineering Program, State University of New York at Binghamton, New York 13902, USA*

[2]*Center for Functional Nanomaterials, Brookhaven National Laboratory, Upton, New York 11973, USA*

(Received 26 October 2021; accepted 21 January 2022; published 3 February 2022)

Alloying element segregation often occurs under a reactive environment but its interplay with the subsequent surface oxidation of the alloy remains unclear. Using synchrotron-based ambient-pressure x-ray photoelectron spectroscopy, we dynamically monitor the surface segregation in $Cu_3Pt(100)$ in response to temperature and oxygen gas. Vacuum annealing leads to surface segregation of Cu along with the enrichment of Pt in the subsurface region. Upon switching to the O_2 atmosphere, dissociative chemisorption of oxygen does not change the surface segregation profile from that under the vacuum annealing condition. A stepwise increase in the oxygen pressure results in the transformation pathway of $Cu \rightarrow Cu_2O \rightarrow CuO$, in which the selective oxidation of Cu gives rise to further accumulation of Pt underneath the oxide/alloy interface that hinders the supply of Cu from the bulk to the oxide/alloy interface, thereby leading to the termination of the surface oxidation after the $Cu_2O \rightarrow CuO$ conversion is completed. This differs from the transformation pathway of $Cu \rightarrow Cu_2O \rightarrow Cu_2O/CuO$ for the oxidation of pure Cu and Cu-Au alloys, in which the oxidation of Cu continues and the Cu_2O/CuO bilayer growth is constantly maintained. These key differences provide useful insight into alloy design for controlling the surface properties such as corrosion resistance and catalytic performance of Cu base alloys.

DOI: 10.1103/PhysRevMaterials.6.025801

I. INTRODUCTION

Many technologically important processes such as corrosion and heterogeneous catalysis are dominated by chemical reactions that happen on alloy surfaces. A microscopic understanding of these chemical processes requires as a prerequisite an atomic-level understanding of the dynamic evolution of element distribution in the surface and subsurface of the alloy. Although bulk alloys have been well studied and phase diagrams delineating the thermodynamic conditions for phase and structure selection are well established, the surface composition of alloys can be quite different from their bulk counterpart. This phenomenon is described as surface segregation resulting from a manifestation of the interplay between thermal and chemical stimuli and kinetic obstacles such as diffusion barriers. The interest in the surface segregation phenomenon is motivated by utilizing this interplay to tune the surface composition and therefore the surface functionality of alloys. For instance, nanoalloys are often used as heterogeneous catalysts; the catalytic process can be promoted or suppressed owing to the surface enrichment of an alloy component. Capitalizing on such effects offers greater flexibility in catalyst design for tuning surface reactivity [1–7]. As a rule of thumb, the element with the lowest surface energy or a larger atom size tends to segregate to the surface for a clean surface, whereas the bonding of adsorbates may induce changes in the surface composition under reactive conditions and the alloy component forming the strongest chemical bond with the adsorbates segregates to the surface. The same driving forces cause segregation to other interfaces, that is, grain boundaries in polycrystal materials and phase boundaries in heterogeneous materials. Therefore, it is usually not possible to predict the properties of alloy surfaces solely on the basis of the bulk composition; the effects of the corresponding environments must be considered. Such fundamental knowledge has great practical importance for manipulating the properties and functionality of the alloys via exploiting the environmental bias. Unfortunately, this level of knowledge is still very limited because understanding the segregation in operating environments not only requires resolving the local composition, but also the ability to capture the dynamic evolution of surface composition/structure under the reaction conditions. Such measurements cannot be achieved with most surface sensitive techniques such as Auger electron spectroscopy (AES), low-energy ion scattering spectroscopy (LEIS), and x-ray photoelectron spectroscopy (XPS) which are typically limited to ultrahigh vacuum (UHV) conditions.

Recent developments in instrumentation have made it possible to investigate the surface and subsurface region in the presence of gases at elevated pressures using the differential pumping mechanism, thus enabling one to bridge the pressure gap. Ambient-pressure (AP) XPS is one of such tools capable of monitoring the chemical states and surface composition at the atomic scale with gas pressures varying from UHV to a few Torr [8] and has been widely used in revealing the atomistic mechanisms of gas-surface reactions [9–14]. In this work, we describe synchrotron-based AP XPS measurements of the surface composition evolution of $Cu_3Pt(100)$ in response to environmental stimuli including high temperature

*gzhou@binghamton.edu

and oxygen gas. The Cu_3Pt binary alloy is chosen for both its fundamental and practical importance. Fundamentally, stoichiometric Cu_3Pt has the ordered $L1_2$ structure and transforms to a substitutionally disordered face-center cubic (fcc) lattice on heating over the bulk order-disorder transition temperature of ∼580 °C [15,16]. The order-disorder transition may have an important implication for studying the surface segregation behavior because of the interplay between surface segregation and chemical ordering, where the former results in the occupation of neighboring lattice sites by the same atomic species at the surface sites whereas the latter causes exactly the opposite. Practically, Cu-Pt alloys show interesting reactivity for various catalytic reactions, among which is an improved activity and selectivity for CO oxidation and hydrocarbon reactions with respect to pure Pt [17–21]. This is surprising since Cu itself is less active than Pt for oxidation and reforming reactions and has been explained controversially in terms of structural and electronic effects [22–26]. The chemical properties of the localized Pt atoms may depend on their coordinating atoms, and a proper interpretation of the catalytic properties of Cu-Pt alloys requires a precise knowledge of surface composition. A Cu_3Pt surface can be a model system for establishing the fundamental principles to control the chemical properties by tuning the surface segregation.

II. EXPERIMENTAL AND COMPUTATIONAL METHODS

AP XPS experiments are performed at the IOS beamline of the National Synchrotron Light Source II (NSLS-II), Brookhaven National Laboratory. The detailed instrument setup was reported previously [27–30]. In short, the multiple differential pumping stages between the main chamber and the hemispherical analyzer allow for continuously acquiring XPS spectra in the presence of gas at pressures of up to ∼5 Torr. The photon energy range of the beamline is from 250 to 2000 eV, which covers O 1*s*, Pt 4*f*, Pt 4*p*, Cu 2*p*, and Cu 3*p* core levels and Cu *LMM* relevant for the current work. The phonon energies greater than 700 eV are adopted in the present work in order to avoid significant changes in the beamline setup for using the lower photon energies that would require switching between two modulators and changing a monochromator grid. Identification of the surface sensitivity of each species in the surface and subsurface regions is performed using depth profiling of the chemical composition by varying the incident photon energy from 400 to 1250 eV. All spectra are collected at the emission angle of 70° between the sample surface normal and the electron analyzer optic axis of the XPS spectrometer. In our *in situ* XPS measurements, the spectral acquisition time varies from 1 to 2 min, depending on the electron energy range of the spectrum. Binding energies in each spectrum are corrected by referring to the Fermi level. XPS spectra are analyzed using a Shirley-type background with the Voigt function. The line shape of a Doniach-Šunjić profile is used to imitate the asymmetry nature of Pt 4*f* features, while a Gaussian-Lorentzian sum formula is used for peak fitting and deconvolution of symmetric peak components in the region of interest. The full width at half maximum (FWHM) is 0.6 eV for Pt $4f7/2$ and $4f5/2$ and 1.55 eV for Cu $3p3/2$ and $3p1/2$. Scofield sensitive factors are introduced into the integrated peak areas of each species in the same binding energy region in order to calculate the relative composition evolution in the corresponding detection depth.

The $Cu_3Pt(100)$ single crystal (99.9999% of purity) is a "top-hat disk" (1 mm thick and 8 mm in diameter), purchased from Princeton Scientific Corp, cut to within 0.1° to the (100) crystallographic orientation and polished to a mirror finish. The pristine crystal is cleaned by repeated cycles of Ar^+ bombardment (5×10^{-5} Torr of Ar, 1 μA cm^{-2}, 1.0 keV, 20 min) at room temperature followed by UHV annealing (550 °C, 10 min). Thereafter, the crystal is held at about 350 °C for several hours to allow bulk and surface ordering to complete. High-purity oxygen (99.9999% of purity) is directly introduced to the sample compartment through a variable-pressure leak valve to tune the surface segregation of Cu atoms.

The density-functional theory (DFT) calculations are performed using the Vienna *ab initio* simulation package (VASP) [31–34]. PW91 generalized gradient approximation (GGA) [35] and projector augmented-wave (PAW) [36] potentials are chosen to describe the electron-electron exchange and core-electron potential separately. The plane-wave cutoff energy is set to be 400 eV and the Brillouin-zone integration is performed using (4×4×1) *K*-point meshes based on Monkhorst-Pack grids. All our calculations are spin averaged, except for isolated molecular and atomic oxygen. In our modeling of the oxygen chemisorbed phases the surface slabs are modeled by five atomic layers with the bottom two layers fixed. Successive slabs are separated by a vacuum space of 12 Å along the direction perpendicular to the surface. The structural optimization is performed by relaxing the positions of all the atoms, except for those of the two bottom layers, until the forces are less than 0.015 eV/Å. As a validity check, our calculated lattice parameter for Cu_3Pt is 3.72 Å, which is in good agreement with previous calculations [37]. All the atomic structures are visualized by using the visualization for electronic and structure analysis (VESTA) program.

III. RESULTS

A. Segregation of the pristine surface during UHV annealing

We first elucidate the surface composition evolution of the $Cu_3Pt(100)$ during UHV annealing (base pressure = 1×10^{-9} Torr), which serves as the baseline to understand the alloy surface in the reactive atmosphere (O_2) shown later. Figure 1(a) presents XPS spectra of the Pt 4*f* and Cu 3*p* regions obtained from the freshly cleaned $Cu_3Pt(100)$ at 100 °C after prolonged annealing at 350 °C in UHV. The incident photon energies of 400 and 1250 eV are used to acquire the XPS spectra, where the difference in the penetration depths of the chosen photon energies allows for probing the chemical composition in the surface and subsurface regions, respectively. As can be seen in Fig. 1(a), the Pt 4*f* peaks are a doublet due to the spin-orbit splitting and consist of $4f7/2$ at 71.0 eV and $4f5/2$ at 74.4 eV. Similarly, the Cu 3*p* also splits into two components with $3p3/2$ at 74.6 eV and $3p1/2$ at 77.2 eV. As shown in Fig. 1(a), the Cu 3*p* spectra partially overlap with the Pt 4*f* region and have a much weaker overall intensity. The relative composition of the two components can be calculated using the ratio of the total areas of each

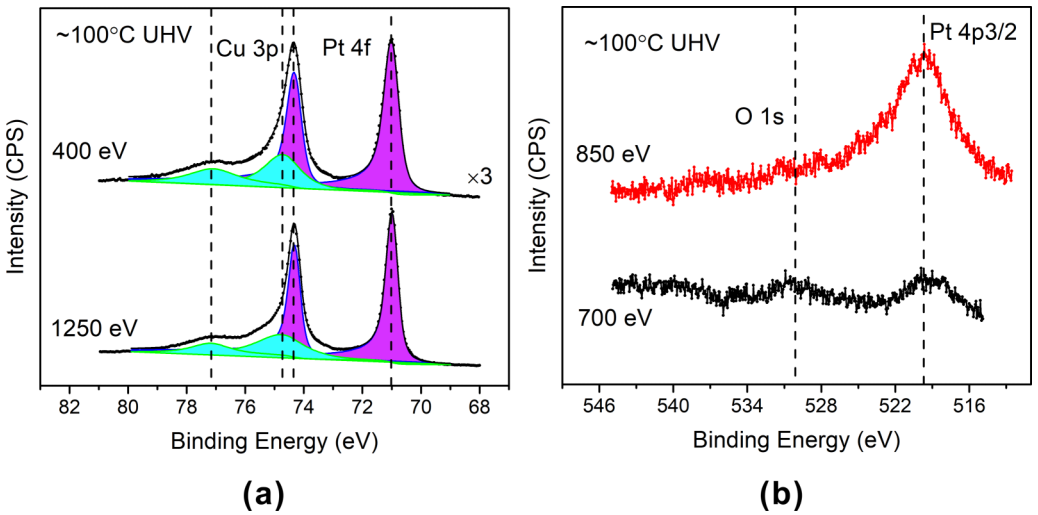

FIG. 1. (a) Pt $4f$ (purple) and Cu $3p$ (cyan) spectra of as-cleaned $Cu_3Pt(100)$ during the UHV annealing at 100 °C. The spectra are obtained using the photon energies of 400 and 1250 eV for detecting the composition difference in the surface and the subsurface regions, respectively. The spectra are normalized to the maximum intensities. (b) O $1s$ and Pt $4p3/2$ spectra of as-cleaned $Cu_3Pt(100)$ taken with the photon energies of 700 and 850 eV, respectively.

component by incorporating the Scofield sensitivity. The Pt composition is found to increase from 37.4 at. % to 40.6 at. % as the photon energy increases from 400 to 1250 eV. For stoichiometric Cu_3Pt, the ideal Pt atomic fraction in the (100) planes of the ordered bulk crystal is alternatively 0.5 and 0 layerwise along the normal plane direction with the overall bulk composition of 25 at. %. The measured Pt compositions for the two incident photon energies are higher than 25 at. %, indicating the Pt enrichment in the probed region.

Figure 1(b) shows an XPS spectrum from the O $1s$ region and confirms that the surface is clean. The O $1s$ locates in the same binding energy region as Pt $4p3/2$ and partially overlaps with the broad Pt peak. A photon energy of 850 eV is used to acquire Pt $4p3/2$, as the kinetic energies of the photoelectrons are similar to that of Pt $4f$ and Cu $3p$ regions probed with the photon energy of 400 eV, yielding the identical sampling depths for these two spectra. The 850 eV spectrum is featureless in the O $1s$ region of ∼530 eV, indicating negligible adsorbed oxygen-containing species. The peak at 520 eV is ascribed to Pt $4p3/2$. The appreciable intensity of Pt $4p3/2$ further confirms the segregation of Pt to the surface region. However, detecting the sample with an even lower photon energy of 700 eV gives only a trace amount of the Pt $4p3/2$ intensity. This indicates that Pt is actually enriched in the subsurface region and the topmost surface layers are dominated by Cu; that is, Pt is depleted from the topmost surface layers and becomes enriched in the subsurface region. Assuming the top layers to be pure Cu and the subsurface layers to be a homogeneous alloy, a two-layer model can be used to analyze the thickness of the Cu segregated layer. Based on the approach by Strohmeier *et al.* [38], the XPS signal intensities from the surface layer (I_{suf}) and the subsurface layer (I_{sub}) are given by

$$I_{suf} = I^0_{suf}\left[1 - \exp\left(-\frac{d}{\lambda\cos\theta}\right)\right], \tag{1}$$

$$I_{sub} = I^0_{sub}\exp\left(-\frac{d}{\lambda\cos\theta}\right), \tag{2}$$

where d is the thickness of the Cu surface layer; θ is the emission angle of the photon electrons, which is 70° in our experiment setup; and λ represents the inelastic free mean path (IMFP) in the surface layer. The incident photon energies of 400 and 1250 eV yield the IMFP of 5.9 and 13.9 Å, respectively, when detecting the emission from the Pt $4f$ and Cu $3p$ regions [39]. I^0 is the electron intensity excited by the incident x ray, which is equal to the concentration of one element modified by corresponding Scofield scattering factors ($\sigma_{Cu2p3/2} = 1.63$, $\sigma_{Cu2p1/2} = 0.848$, $\sigma_{Pt4f7/2} = 8.65$, $\sigma_{Pt4f5/2} = 6.8$). Assuming the subsurface Pt concentration to be C_{Pt}, the detected signal intensity ratio can be expressed as

$$\frac{I_{Cu}}{I_{Pt}} = \frac{I_{Cu,suf} + I_{Cu,sub}}{I_{Pt,\ sub}} = \frac{I_{suf} + (1 - C_{Pt})I_{sub}}{C_{Pt}I_{sub}} = \frac{I^0_{Cu}}{I^0_{Pt}}\frac{1 - C_{Pt}\exp(-d/\lambda\cos\theta)}{C_{Pt}\exp(-d/\lambda\cos\theta)}; \tag{3}$$

thus, the thickness of the top Cu layer is

$$d = \lambda\cos\theta\left\{\ln\left[C_{Pt}\left(1 + \frac{I_{Cu}I^0_{Pt}}{I_{Pt}I^0_{Cu}}\right)\right]\right\}. \tag{4}$$

The pure Cu layer thickness can be calculated using Eq. (4) with the peak areas from Fig. 1(a). The photon energy of 400 eV yields a pure Cu layer no more than 2.0 Å in thickness, while the photon energy of 1250 eV yields a thickness of 4.1 Å at the maximum. These thicknesses are equivalent to the topmost—one to two atomic layers of Cu_3Pt with the $L1_2$ ordering on the basis of a fcc lattice with the lattice parameter of 3.7 Å.

By combining Cu $3p$, Pt $4f$, and Pt $4p$ probed with the different incident photon energies, the measured segregation profile can be divided into three regions. That is, nearly pure Cu in the topmost two layers, Pt enrichment in the subsurface with a Pt composition ranging from 37.4 at. % (measured with the photon energy of 400 eV) to 40.6 at. % (with 1250 eV) (these values are averaged including the topmost two layers

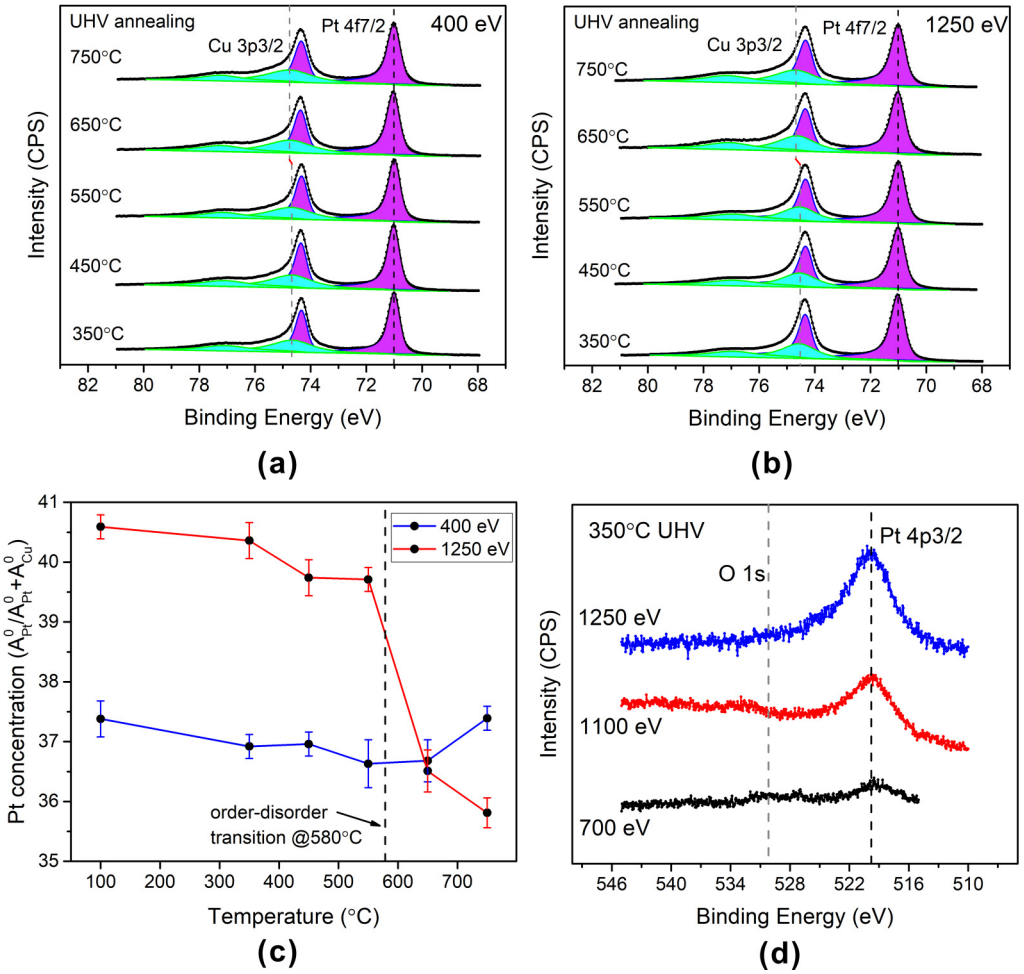

FIG. 2. (a), (b) Pt 4f (purple) and Cu 3p (cyan) spectra of $Cu_3Pt(100)$ taken with the photon energies of 400 and 1250 eV during the UHV annealing from 350 °C to 750 °C, where the spectra are normalized to the maximum intensities. (c) Evolution of the Pt concentration as a function of the annealing temperature, where the error bars represent the variations based on the time series adjacent XPS spectra, and the small errors indicate the relatively steady state of the surface composition. (d) O 1s and Pt 4p3/2 spectra measured at 350 °C with various photon energies.

of pure Cu), and the bulk region with the stoichiometric Pt composition of 25%. Since the signal detected by XPS is the accumulation of weighted intensity from various depths of the sample, we assign the spectra taken with the photon energy of 400 eV as the "surface region", which includes the pure Cu surface and a few layers from the Pt-enriched subsurface, and spectra taken with the photon energy of 1250 eV as the "subsurface region", which includes the pure Cu surface and more layers from the Pt-enriched subsurface. It can be noted from Fig. 1(b) that the O 1s region obtained with the photon energy of 700 eV shows some diminutive intensity, which may be caused by the presence of a trace amount of surface oxygen. The effect from this trace amount of oxygen impurity is negligible on the segregation profile for a clean surface. This is confirmed later in Fig. 2, showing that the O 1s intensity disappears completely after annealing the crystal to 350 °C whereas the segregation profile remains nearly the same.

The above composition profile measured at a relatively low temperature (∼100 °C) serves as a baseline for evaluating the temperature effect on the surface segregation. Cu_3Pt has the $L1_2$ type of ordered structure with the bulk order-disorder phase transition at $T = 580$ °C. We thus measure the surface segregation behavior for both the order and disorder phases by annealing the Cu_3Pt crystal under UHV from 350 °C to 750 °C with a temperature interval of 100 °C. The crystal is kept at each temperature for more than 20 min for reaching composition equilibrium during the XPS measurements. Figures 2(a) and 2(b) show the XPS spectra of Pt 4f and Cu 3p peaks obtained with the incident photon energies of 400 and 1250 eV, respectively, where the surface segregation reaches a steady state at each temperature, as confirmed by the saturated intensity of the Pt 4f7/2 peaks with a longer annealing time at the temperature. The position of the Pt 4f7/2 peaks stays constant at the different temperatures whereas Cu 3p3/2 peaks shift slightly toward the higher binding energy by ∼0.15 eV at 650 °C and 750 °C when detected with the photon energy of 1250 eV for the subsurface region [Fig. 2(b)]. This binding energy shift can be caused by the order-disorder transition in Cu_3Pt, for which the increased compositional disordering in the bulk changes the chemical environment of Cu atoms and thus induces the chemical shift. By contrast, there is only a 0.07 eV shift of the Cu 3p3/2 spectra probed with

the photon energy of 400 eV for the surface region [Fig. 2(a)]. This can be related to the Cu surface segregation that occurs at the lower annealing temperature of 100 °C, as shown in Fig. 1. The difference in the binding energy shifts measured with the two photon energies confirms that the chemical environment varies from the surface to the subsurface region and the surface region is already enriched with Cu at the temperatures well below the bulk order-disorder transition point, for which the bulk order-disorder transition does not induce significant changes in the chemical environment to the surface region.

The evolution of the integrated peak areas of Pt $4f$ and Cu $3p$ can be quantified to determine the composition evolution in the surface and subsurface regions under the UHV annealing at different temperatures. Figure 2(c) illustrates the XPS-measured composition of Pt as the crystal is annealed from 100 °C to 750 °C, which shows that the Pt concentrations stay relatively constant at ∼37.4 at. % (measured with the photon energy of 400 eV) and ∼40.6 at. % (measured with 1250 eV) for the subsurface region at the temperatures below the order-disorder transition point. After passing the order-disorder transition temperature, the subsurface shows a slightly increased Pt concentration of ∼37.5 at. % measured with 400 eV but a large drop of the Pt concentration to ∼35.6 at. % measured with 1250 eV at 750 °C. Since the smaller photon energy of 400 eV probed a shallower depth than the higher photon energy of 1250 eV, the trend in Fig. 2(c) indicates that the shallow subsurface region has a relatively stable concentration across the different temperatures, and the slightly increased Pt at 750 °C can be attributed to the rejection of the remaining Pt atoms in the outermost surface layers to the adjacent subsurface region. By contrast, the measurements with the larger photon energy of 1250 eV indicate Pt desegregation in the deeper subsurface region above the order-disorder transition temperature. That is, the order-disorder transition in the bulk tends to drive the composition homogenization between the deeper subsurface region and the bulk via inward diffusion of accumulated Pt in the deeper subsurface region to the bulk. Meanwhile, the topmost atomic layers are confirmed to maintain as pure Cu above the order-disorder transition temperature. Similar to Fig. 1(b), the O $1s$ and Pt $4p3/2$ region taken at 350 °C with the photon energy of 700 eV shows the absence of O signal with a trace amount of Pt signal [Fig. 2(d)], suggesting that the surface is free of adsorbed O and the topmost layers remain as nearly pure Cu. The Pt $4p3/2$ peak emerges stronger in intensity with the higher photon energies of 1100 and 1250 eV, indicating the higher Pt concentration in the subsurface region.

B. Surface segregation during O_2 annealing

The above measurements demonstrate that the UHV annealing results in the surface segregation of Cu from the subsurface region, which in turn induces the Pt accumulation in the subsurface region by the inward rejection of surface Pt to the subsurface along with the outward migration of Cu toward the surface. This provides the baseline to understand the surface composition evolution during the O_2 annealing. Since the surface is already enriched with Cu from the UHV annealing, switching to the O_2 atmosphere may induce more Cu segregation to the surface region due to the high O affinity of Cu, thereby resulting in further Pt enrichment in the subsurface region. Figures 3(a) and 3(b) show Pt $4f$ and Cu$3p$ spectra obtained at 350 °C with the photon energies of 400 and 1250 eV, where the freshly cleaned sample is first annealed in UHV to reach equilibrium before oxygen gas is introduced into the vacuum chamber with the stepwise increase in oxygen pressure (pO_2) from 1×10^{-4} to 1×10^{-1} Torr. The sample is kept at each pO_2 for more than 20 min to ensure the saturated O coverage, as confirmed by monitoring the intensity evolution of the O $1s$ spectra.

The O_2 exposure at low pO_2 (1×10^{-4} and 1×10^{-3} Torr) results in chemisorbed O on the Cu-terminated surface. As shown in Fig. 3(a), the binding energy of Cu $3p$ shifts slightly from 74.6 eV (under UHV) to 74.8 eV with the presence of chemisorbed O in $pO_2 = 1 \times 10^{-4}$ and 1×10^{-3} Torr. Increasing pO_2 to 1×10^{-2} Torr leads to the oxidation of Cu to Cu_2O with the shift of the binding energy of Cu $3p$ to 75.1 eV. Further increase in pO_2 to 1×10^{-1} Torr results in the formation of CuO, which is accompanied with the shift of the Cu $3p$ peak to 75.9 eV. These chemical shifts as a function of the oxidation state of Cu are consistent with previous studies on the oxidation of pure Cu [40]. As shown in Fig. 3(b), the shift of the binding energies of the Cu $3p$ measured with the photon energy of 1250 eV shows the same dependence on pO_2 as the measurements made with the lower photon energy of 400 eV [Fig. 3(a)]. As can be seen from Figs. 3(a) and 3(b), the binding energy of Pt $4f$ stays unchanged, irrespective of the changes in pO_2. This means that Pt $4f$ is insensitive to the chemical environment of Pt atoms in the alloy [41,42], which is further confirmed in Figs. 2(a) and 2(b), illustrating that the binding energy of Pt $4f$ maintains constant during the Pt enrichment in the subsurface (driven by surface segregation of Cu) and the subsequent Pt migration from the subsurface to deeper atomic layers (driven by the composition homogenization) above the bulk order-disorder transition temperature. This is also in line with other XPS measurements, showing that the binding energy of Pt $4f$ for alloyed Pt is independent of alloy compositions.

Figure 3(a) shows that there is a slight decrease in the intensities of Pt $4f$ and Cu $3p$ spectra after the surface is covered by chemisorbed O in the low pO_2 of 1×10^{-4} and 1×10^{-3} Torr. The further stepwise increase in pO_2 leads to the formation of Cu_2O at $pO_2 = 1 \times 10^{-2}$ Torr and then CuO at $pO_2 = 1 \times 10^{-1}$ Torr, where the remarkable reduction of the overall intensity of the spectra is caused by inelastic scattering of the photoelectrons due to the significant presence of gas molecules at the higher pO_2. Notably, the Cu_2O component is absent in the Cu $3p$ spectra at $pO_2 = 1 \times 10^{-1}$ Torr, suggesting that the CuO growth involves consuming the Cu_2O formed at $pO_2 = 1 \times 10^{-2}$ Torr. Meanwhile, the intensity for Pt $4f$ becomes barely visible at $pO_2 = 1 \times 10^{-1}$ Torr, indicating the growth of a relatively thick CuO overlayer that attenuates the XPS signal from Pt atoms underneath the oxide/alloy interface. The supply of Cu atoms from the Cu_3Pt substrate for the external oxide growth leads to the enrichment of Pt atoms underneath the oxide/alloy interface that can be probed by the depth profiling using the higher photon energy of 1250 eV to reach the deeper region. This is illustrated

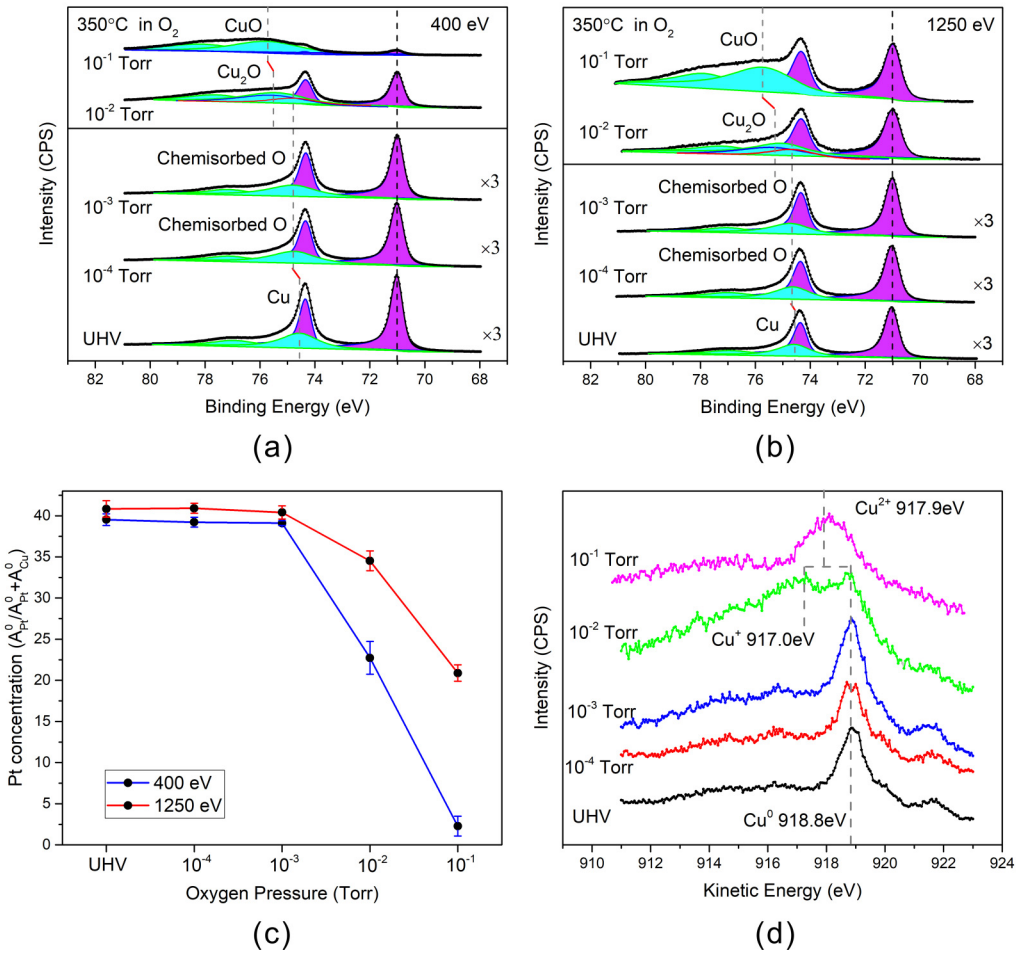

FIG. 3. (a), (b) Pt $4f$ (purple) and Cu $3p$ (cyan) spectra of $Cu_3Pt(100)$ measured with the photon energies of 400 and 1250 eV, respectively. The crystal is annealed at 350 °C, first in UHV and then in the O_2 atmosphere with the stepwise increase in pO_2 from 1×10^{-4} to 1×10^{-1} Torr 350 °C. The spectra shown correspond to a relatively steady state with the saturated peak intensity at each pO_2. To compare the actual intensities, the peak heights of the spectra acquired in UHV and $pO_2 = 1 \times 10^{-4}$ to 1×10^{-3} Torr should be multiplied by a factor of 3. (c) Pt concentration evolution as a function of pO_2 at 350 °C, where the error bars represent the variations based on the time series adjacent XPS spectra (the small errors indicate the relatively steady state of the surface composition). (d) Cu *LMM* Auger emission measured as a function of pO_2 at 350 °C and with the photon energy of 1250 eV.

in Fig. 3(b), showing that the intensity of the Cu $3p$ spectra becomes stronger upon the increase in pO_2 from 1×10^{-2} to 1×10^{-1} Torr, where the increased loss of the photoelectron counts due to inelastic scattering by gas molecules at the higher pO_2 is outcompeted by the contribution from the oxide thickening. Despite the increased inelastic scattering by gas molecules upon the increase in pO_2 from 1×10^{-2} to 1×10^{-1} Torr, it can be noted from Fig. 3(b) that there is no obvious intensity drop for the Pt $4f$ spectra, illustrating the progressive Pt enrichment underneath the oxide/alloy interface upon the thickening of the CuO overlayer by the outward diffusion of Cu in the substrate.

Figure 3(c) shows the Pt concentration evolution by quantifying the peak area of Cu $3p$ and Pt $4f$ spectra shown in Figs. 3(a) and 3(b). It can be seen that O chemisorption from the O_2 dosing at the low pO_2 of 1×10^{-4} and 1×10^{-3} Torr does not yield more surface segregation of Cu and the Pt concentration remains nearly the same as that in the UHV annealing. Figure 3(c) shows that a dramatic decrease in the Pt/Cu ratio occurs after raising pO_2 to 1×10^{-2} and 1×10^{-1} Torr, during which the Cu is sequentially oxidized to Cu_2O and CuO, respectively. It can also be noted from Fig. 3(c) that the measurements with the higher photon energy of 1250 eV Pt yield the higher Pt/Cu ratios compared with that by the photon energy of 400 eV. This is because the higher photon energy has the larger probing depth to reach the deeper subsurface region that is enriched with Pt atoms underneath the oxide/alloy interface.

The changes in the oxidation state of Cu as a function of pO_2 are also confirmed by *LMM* Auger spectra as shown in Fig. 3(d). For the clean surface in the UHV, the Auger electrons have the kinetic energy of 918.8 eV, which corresponds to metallic Cu (Cu^0). For the O_2 annealing at the low pO_2 of 1×10^{-4} and 1×10^{-3} Torr, the Auger electrons have the same kinetic energy of 918.8 eV, indicating that Cu still largely maintains the metallic state despite the presence of chemisorbed O at the surface. After raising pO_2 to 1×10^{-2} Torr, a new intense peak with the kinetic energy of 917.0 eV becomes evident, corresponding to Cu^+ in Cu_2O. It can be also noted that the peak (918.8 eV) corresponding to metallic

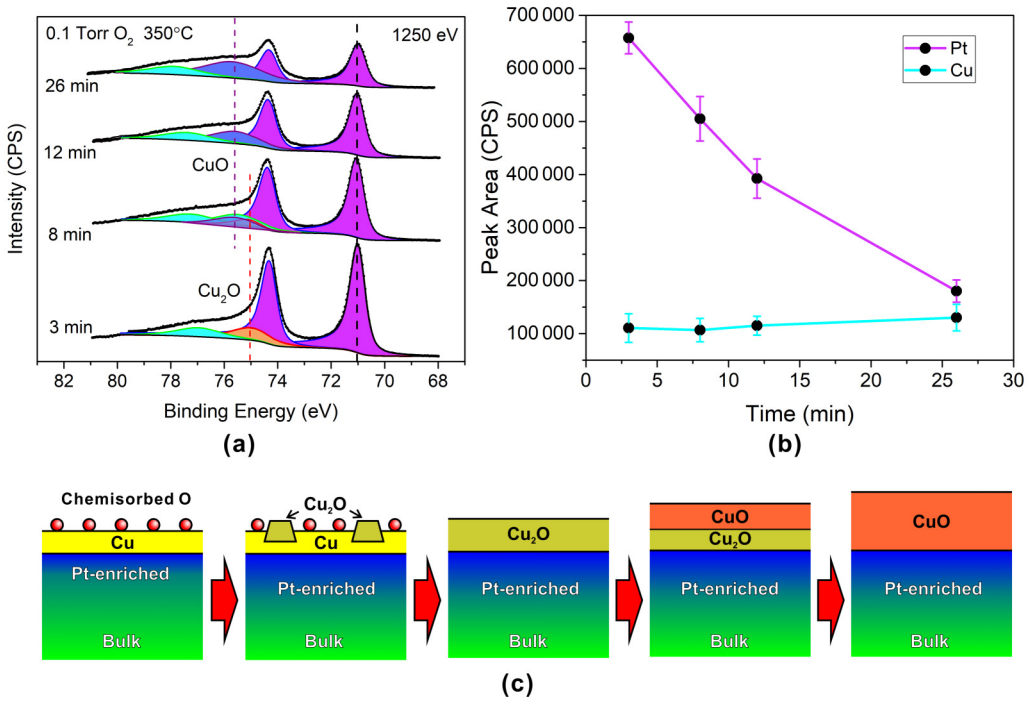

FIG. 4. (a) Time sequence of Pt $4f$ (purple) and Cu $3p$ (cyan) spectra obtained from $Cu_3Pt(100)$ during the O_2 annealing at $pO_2 = 1 \times 10^{-1}$ Torr and 350 °C, where the spectra are normalized to the background. The Cu $3p3/2$ spectra are further deconvoluted into the Cu_2O (orange) and CuO (blue) components. (b) Intensity evolution of the Pt $4f$ and Cu $3p$ spectra shown in (a), where the relatively larger error bars based on the time series adjacent XPS spectra indicate the enhanced reaction kinetics at the higher pO_2 that gives rise to the relatively faster changes in the surface composition. (c) Schematic illustrating the transformation pathway of chemisorbed O → Cu_2O → CuO and the resulting Pt enrichment underneath the oxide/alloy interface.

Cu is still visible, indicating that the oxidation occurs via the nucleation and growth of Cu_2O islands, where the observed Cu^+ peak is associated with Cu_2O islands whereas the metallic Cu peak is associated with the unoxidized areas between Cu_2O islands. This corroborates extensive *in situ* electron microscopy observations showing that the early-stage oxidation of Cu and Cu alloys such as Cu-Au and Cu-Pt is controlled by the nucleation and growth of Cu_2O islands [43–47]. Further increase in pO_2 to 1×10^{-1} Torr results in the peak shift to the kinetic energy of 917.9 eV, corresponding to Cu^{2+} in CuO. It can also be noted from Fig. 3(d) that the metallic Cu and Cu^+ peaks disappear at $pO_2 = 1 \times 10^{-1}$ Torr, indicating that the entire surface is now fully covered with the CuO by consuming the Cu_2O formed at the lower pO_2 of 1×10^{-2} Torr. This is consistent with the measurements made by monitoring the evolution of Cu $3p$ spectra as a function pO_2, showing the Cu_2O formation at $pO_2 = 1 \times 10^{-2}$ Torr and its complete transformation to CuO after prolonged O_2 exposure at $pO_2 = 1 \times 10^{-1}$ Torr [Figs. 3(a) and 3(b)].

The $Cu_2O \rightarrow$ CuO transformation process is illustrated by monitoring the temporal evolution of Cu $3p$ and Pt $4f$ spectra acquired during the O_2 flow at $pO_2 = 1 \times 10^{-1}$ Torr and 350 °C. As shown in Fig. 4(a), the Cu $3p$ spectra are dominated by Cu_2O after 3 min of the O_2 exposure, where the absence of the metallic component of Cu indicates that the surface is fully covered by Cu_2O via the coalescence of Cu_2O islands as described above in Fig. 3. After 8 min of the O_2 flow, the Cu $3p3/2$ peak shifts from 75.1 to 75.6 eV, which can be further deconvoluted to two peaks ascribed to CuO and Cu_2O, respectively, indicating the coexistence of CuO and Cu_2O. Upon continued O_2 exposure, the Cu_2O component becomes increasingly invisible (12 min) and disappears completely (26 min), at which time the Cu $3p3/2$ peak is stabilized at the binding energy of 75.9 eV, which matches well the binding energy for stochiometric CuO [48]. With the constant temperature and pO_2, the XPS intensities only depend on the scattering factor of the elements being detected, so the spectra can be normalized to the same background level. Hence, the temporal intensity evolution of the Cu $3p$ and Pt $4f$ spectra is quantified by monitoring the peak area changes to reflect the oxidation kinetics. Figure 5(b) illustrates the measured peak area evolution of Cu $3p$ and Pt $4f$ as a function of the O_2 exposure at $pO_2 = 1 \times 10^{-1}$ Torr and 350 °C. Surprisingly, the Cu amount stays nearly constant throughout the whole oxidation process whereas the Pt intensity decreases markedly. The little change in the Cu content indicates that the CuO growth occurs via consuming the existing Cu_2O without involving the supply of new Cu from the Cu_3Pt substrate in spite of the continued O_2 exposure. The weakening of the Pt signal is caused by the $Cu_2O \rightarrow$ CuO transformation induced thickening of the oxide layer (the c lattice parameters are 4.27 and 5.13 Å for Cu_2O and CuO, respectively). Therefore, the Pt enrichment underneath the oxide/alloy interface works as a protective barrier to significantly slow down the supply of Cu atoms from the Cu_3Pt substrate for new oxide formation. Figure 4(c) illustrates schematically the entire oxidation process starting with the chemisorbed O layer, nucleation and growth of Cu_2O islands, and the $Cu_2O \rightarrow$ CuO transformation, toward the

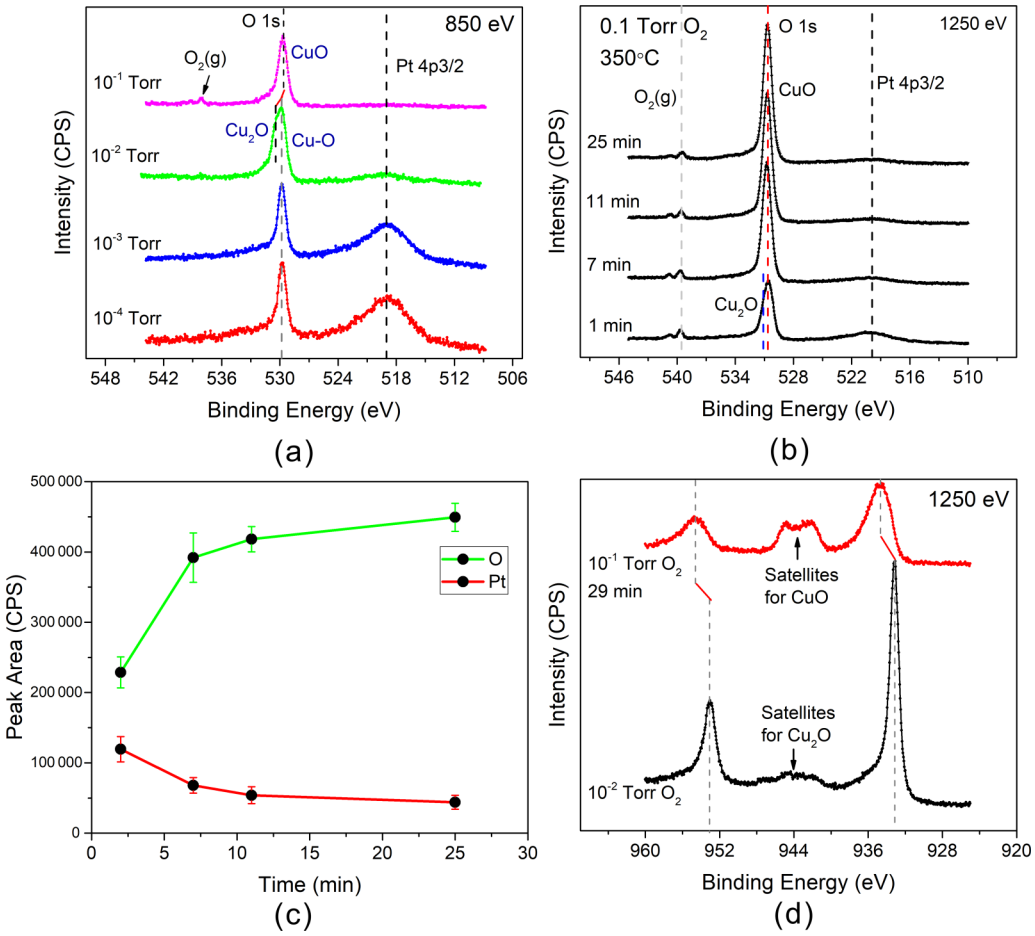

FIG. 5. (a) Evolution of O 1*s* and Pt 3*p*3/2 spectra obtained with the incident photon energy of 850 eV during the O_2 annealing of $Cu_3Pt(100)$ at 350 °C with the stepwise increase in pO_2; spectra are normalized to the maximum intensities. (b) Time sequence of O 1*s* and Pt 3*p*3/2 spectra obtained with the incident photon energy of 1250 eV during the O_2 exposure at $pO_2 = 1 \times 10^{-1}$ Torr and 350 °C; spectra are normalized to the same background. (c) Intensity evolution of the O 1*s* and Pt 3*p*3/2 spectra shown in (b). The error bars represent the variations based on the time series adjacent XPS spectra. (d) Cu 2*p* spectra measured during the O_2 annealing at 350 °C with $pO_2 = 1 \times 10^{-2}$ Torr and $pO_2 = 1 \times 10^{-1}$ Torr, respectively.

oxidation termination due to the selective oxidation of Cu-induced Pt enrichment underneath the oxide/alloy interface that limits the supply of Cu from the substrate.

The oxidation-induced composition evolution of $Cu_3Pt(100)$ described in Figs. 3 and 4 is based on monitoring the Pt 4*f* and Cu 3*p* spectra; more information can be derived from the O 1*s* and Pt 3*p* regions. By using the photon energy of 850 eV, the kinetic energy of photoelectrons from the O 1*s* and Pt 3*p* regions is identical to the spectra of Pt 4*f* and Cu 3*p* taken with 400 eV photon energy [Fig. 3(a)], thereby giving the similar sampling depth for comparison. Figure 5(a) shows O 1*s* and Pt 4*p*3/2 spectra taken with the photon energy 850 eV during the O_2 annealing at 350 °C [the same condition as Fig. 3(a)]. The Pt/O ratio derived from the peak intensities in Fig. 5(a) can be combined with the Cu/Pt ratio in Fig. 3(c), giving the Pt/Cu/O ratios of 40/60/0, 27/42/31, 26/40/34, and 8/38/54 under UHV first, and then in $pO_2 = 1 \times 10^{-4}$, 1×10^{-3}, and 1×10^{-2} Torr O_2, respectively. These ratios show that the surface is Cu rich under UHV, consistent with the measurements in Figs. 1 and 2. Upon switching to the O_2 atmosphere, the surface is first covered with chemisorbed O in $pO_2 = 1 \times 10^{-4}$ and 1×10^{-3} Torr, and it is then oxidized to Cu_2O after the oxygen pressure is increased to $pO_2 = 1 \times 10^{-2}$ Torr. However, the Cu content maintains relatively constant at ~40% regardless of the transition from chemisorbed O to Cu_2O at the higher pO_2, indicating that the surface does not oxidize beyond the Pt-rich subsurface region because the latter serves as the protective barrier to block the outward diffusion of Cu. This is also consistent with the measurements by Pt 4*f* and Cu 3*p* spectra in Fig. 4(b), showing that there is only very little change in the Cu content even after the Cu_2O is fully converted into CuO at the higher pO_2 of 1×10^{-1} Torr.

The $Cu_2O \rightarrow CuO$ transformation during the O_2 exposure at $pO_2 = 1 \times 10^{-1}$ Torr and 350 °C is also monitored using O 1*s* and Pt 3*p*3/2. As shown in Fig. 5(b), the time-sequence spectra are acquired with the photon energy of 1250 eV that provides a larger sampling depth to detect the evolution of the Pt content underneath the oxide/alloy interface. In the beginning of the sequence (1 min), the O 1*s* shows that the surface is already dominated by CuO with a tiny signature of Cu_2O at the higher binding energy side. Upon the continued O_2 exposure, the Cu_2O is continuously converted into CuO,

which is accompanied with the increase in the O 1*s* intensity because of the higher O content in CuO. Figure 5(c) illustrates the intensity evolution of the O 1*s* as a function of the O_2 exposure time, showing that the O 1*s* intensity approaches saturation after 7 min as the $Cu_2O \rightarrow CuO$ conversion approaches completion. The saturation in the O 1*s* intensity signals the termination of the surface oxidation owing to the lack of supply of additional Cu from the substrate. This is in accord with the observation in Fig. 4(b) showing the saturated Cu content irrespective of further O_2 exposure. It can be also noted from Fig. 5(c) that the intensity of the Pt $3p3/2$ spectra decreases to a lower plateau level. This correlates well with the O 1*s* intensity evolution, for which the initial intensity reduction of the Pt $3p3/2$ is caused by the thickening of the oxide layer due to the $Cu_2O \rightarrow CuO$ conversion and the plateau level corresponds to the completion of the conversion. Figure 5(d) shows Cu 2*p* spectra measured in $pO_2 = 1 \times 10^{-2}$ and 1×10^{-1} Torr, in which the satellite features between two spin-split main peaks are a "fingerprint" of the Cu_2O and CuO components, respectively.

IV. DISCUSSION

The Cu-Pt system has been studied as a model system for understanding segregation phenomena. Most of the reported surface-science studies of extended surfaces of single crystals were devoted to the equilibrium segregation profile under UHV annealing and showed a tendency for Cu surface segregation. Shen *et al.* reported LEIS analysis on $Cu_3Pt(100)$, (110), and (111) [22–24], showing that the surface layers consist of Cu/Pt with the atomic ratios of 100/0, 82/18, and 80/20 for these three low-index planes, respectively. However, as described above, the elemental enrichment in Cu_3Pt changes from being Cu rich in the surface to Pt rich in the subsurface. Due to uses of different experimental techniques, some controversial conclusions of Pt surface segregation instead of Cu segregation were also reported in the literature [25,26,49].

Our AP XPS measurements demonstrate that the UHV annealing of $Cu_3Pt(100)$ results in the surface segregation (approximately the two topmost layers) of Cu along with the enrichment of Pt in the subsurface. Surface segregation may be driven by differences in surface energies between alloy components or by the relief of bulk lattice strain due to atomic size mismatch. That is, the component with a lower surface energy tends to segregate to the surface to minimize the surface energy or larger atoms are favored on the surface because the surface can relax to accommodate them better than is possible in the bulk. In the Cu-Pt system, the difference in the atomic radii is ~8% ($r_{Cu} = 1.27$ Å and $r_{Pt} = 1.39$ Å), for which Pt atoms are favored on the surface. However, Cu has a smaller surface energy than pure Pt ($\sigma_{Cu(100)} = 1.96\,J/m^2$, $\sigma_{Pt(100)} = 2.48\,J/m^2$) [50], which favors the surface segregation of Cu rather than Pt. The competing interplay of the opposing effects between the two driving forces is manifested from the measured composition profile shown above, where the smaller surface energy of Cu outcompetes with the relief of the lattice strain and drives the surface segregation of Cu atoms from the subsurface. In turn, the enrichment of Pt in the subsurface region is thus expected due to the exchange of surface Pt with subsurface Cu.

Upon switching from UHV to the O_2 atmosphere at the relatively low pO_2 of 1×10^{-4} and 1×10^{-3} Torr results in the dissociative chemisorption of O_2 on the $Cu_3Pt(100)$ surface. As shown in Fig. 3, the presence of chemisorbed O does not change the surface segregation profile from that under the UHV condition. It is instructive to compare this behavior to $Cu_3Au(100)$, for which the low pO_2 of 1×10^{-6} Torr provides the sufficient chemical driving force to flip the surface termination from being Au rich under the UHV annealing to Cu rich in the O_2 annealing [27]. This difference in their response to the O_2 exposure between $Cu_3Au(100)$ and $Cu_3Pt(100)$ lies in their surface termination from the UHV annealing. For $Cu_3Au(100)$, the smaller surface energy of Au drives the segregation of Au atoms to the surface under the UHV annealing, resulting in the Au-terminated surface with Cu enrichment in the subsurface. A switch to the O_2 atmosphere drives the surface segregation of Cu from the subsurface due to its larger affinity with O. By contrast, the UHV annealing of $Cu_3Pt(100)$ induces the surface segregation of Cu, producing the Cu surface termination with Pt enrichment in the subsurface, as shown in Figs. 1 and 2. The presence of chemisorbed O on the $Cu_3Pt(100)$ during the O_2 annealing at the low pO_2 (1×10^{-4} and 1×10^{-3} Torr) does not change the surface composition because the surface is already terminated by Cu from the UHV annealing.

The above measurements indicate that the O chemisorption on the Cu-terminated $Cu_3Pt(100)$ does not induce the surface segregation of additional Cu from the subsurface, suggesting that the Pt-rich sublayer serves as a protective barrier to the oxygen attack. This is further confirmed by DFT modeling of the O chemisorption on the Cu-terminated $Cu_3Pt(100)$, as shown in Fig. 6. Similar to the O adsorption on the Cu(100) surface [51], our DFT calculations show that the fourfold hollow sites are the most favorable sites for O adsorption on the Cu-terminated $Cu_3Pt(100)$ surface, which yield the lowest adsorption energy −1.86 eV. Figure 6(a) shows the relaxed surface with the O coverage of 0.25 monolayer (ML). By swapping a Pt atom in the second layer with a Cu atom in the third layer, we observe an increase in the total system energy by 0.56 eV, indicating the unfavorable tendency for the segregation of Cu from deeper layers to the sublayer. Figure 6(b) illustrates the surface with 0.5 ML of O coverage, showing the slight upward relaxation (by ~0.18 Å) of the topmost layer. Similarly, the swapping between a Pt atom in the second layer and a Cu atom in the third layer leads to an increased system energy by 0.50 eV. Figure 6(c) corresponds to the surface with 0.75 ML of O coverage, in which the exchange between the Pt atom in the second layer and the Cu atom in the third layer still results in an increased system energy by 0.47 eV. Figure 6(d) illustrates the fully relaxed structure at the O coverage of 1 ML, showing that some of the O and Cu atoms in the topmost layer undergo large upward relaxation that results in the separation of Cu and O along the vertical direction. Figure 6(e) illustrates the bonding configuration of Cu atoms with the coordinating O atoms, and our measurements show that the resultant Cu-O bond lengths range from 1.86 to 2.08 Å and the Cu-O-Cu bond angles fall into the range of 92.2°–123.4°. According to our DFT calculations, the corresponding bond

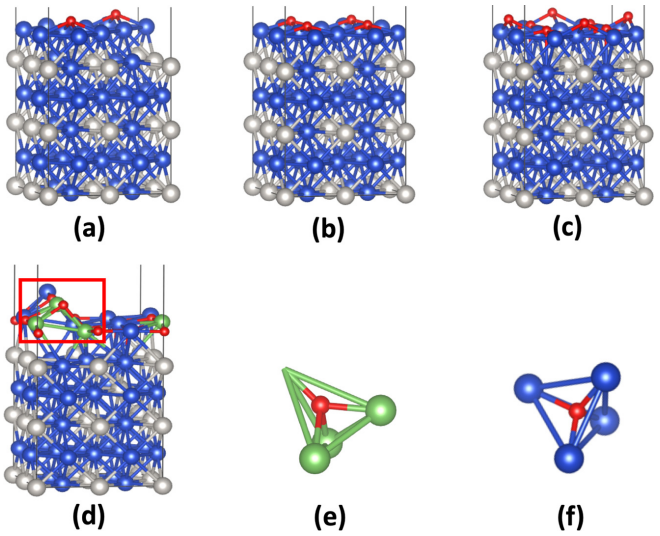

FIG. 6. DFT simulations of O adsorption on the Cu-terminated $Cu_3Pt(100)$ surface as a function of oxygen coverage of (a) 0.25 ML, (b) 0.5 ML, (c) 0.75 ML, and (d) 1 ML, respectively. (e) Enlarged view of the Cu-O bonding configuration marked with the red box in (d). (f) Perspective view of the Cu-O bond configuration in bulk Cu_2O. Red, blue, and gray spheres represent O, Cu, and Pt atoms, respectively; green spheres represent the Cu atoms forming the Cu-O tetrahedron.

length and bond angle in bulk Cu_2O are 1.86 Å and 109.47°, respectively [Fig. 6(f)]. It is clear that the resultant Cu-O bond configuration strikingly resembles that of the bulk phase of Cu_2O, which signals the onset of Cu_2O nucleation at the O coverage of 1 ML. Meanwhile, our DFT calculations show that the system energy decreases by 0.57 eV by exchanging the Pt atom in the second layer with the Cu atom in the third layer, indicating a tendency for the migration of Pt toward deeper atomic layers upon the Cu_2O formation induced by the progressive O uptake. This prediction is consistent with our AP XPS measurements showing the decreased Pt concentration in the shallow subsurface region after the Cu_2O formation at the higher pO_2 of 1×10^{-2} Torr (Figs. 3–5).

The DFT results above show that 1 ML of the O coverage is needed to initiate the nucleation of Cu_2O on $Cu_3Pt(100)$. This is in contrast to Cu(100) that shows the $(2\sqrt{2} \times \sqrt{2})R45°$ missing-row reconstruction at 0.5 ML of O coverage [52] and the $c(3\sqrt{2} \times \sqrt{2})R45°$ reconstruction with 2/3 ML of O coverage, where the latter can be described as $Cu_2O(100)$ [53]. The higher O coverage required for the Cu_2O formation can be ascribed to the presence of Pt in the subsurface that blocks the inward migration of adsorbed O and the outward migration of Cu atoms from the deeper atomic layers. This blocking effect is further manifested in the later stages of the oxide growth and leads to the significant difference from the oxidation of pure Cu. As shown in Figs. 4 and 5, the $Cu_3Pt(100)$ surface is sequentially oxidized into Cu_2O and CuO upon the stepwise increase in pO_2 from 1×10^{-2} to 1×10^{-1} Torr, where the CuO growth occurs via the $Cu_2O \rightarrow$ CuO transformation. The observed sequential formation of Cu_2O and CuO is consistent with the oxidation pathway of pure Cu that results in the CuO/Cu_2O bilayer growth with CuO being the top layer via the outward diffusion of Cu from the metallic substrate through the CuO/Cu_2O overlayer to adsorbed O for new oxide formation at the CuO surface [29,54]. However, a significant difference exists in the CuO growth between the oxidation of pure Cu and $Cu_3Pt(100)$. The oxidation of pure Cu follows the transformation pathway of $Cu \rightarrow Cu_2O \rightarrow Cu_2O/CuO$ [29], in which the CuO/Cu_2O bilayer oxide growth occurs simultaneously at the O_2/CuO and CuO/Cu_2O interfaces. That is, CuO grows at the outer surface via the reaction between chemisorbed O at the CuO surface and arriving Cu atoms supplied by the outward diffusion from the Cu substrate. The inner Cu_2O layer grows at the expense of the CuO layer at the Cu_2O/CuO interface, where the O-richer CuO decomposes and thus provides the necessary O for reacting with arriving Cu atoms supplied from the Cu substrate. Because the diffusivity of Cu in CuO is smaller than that in Cu_2O [55,56], the Cu_2O layer is much thicker than the CuO layer, as shown from many experimental observations [54,57]. By contrast, the CuO growth during the oxidation of $Cu_3Pt(100)$ does not involve much growth of the inner Cu_2O layer. As shown in Figs. 4 and 5, the continued O_2 exposure at $pO_2 = 1 \times 10^{-1}$ Torr results in the complete conversion of Cu_2O to CuO by following the transformation pathway of $Cu \rightarrow Cu_2O \rightarrow CuO$. In this reaction sequence, there is no much new Cu_2O formation at the Cu_2O/CuO interface during the $Cu_2O \rightarrow CuO$ transformation, as evidenced by the relatively constant amount of Cu throughout the whole transformation process. This reaction sequence leads to the termination of the oxidation after the complete transformation of Cu_2O into CuO, which differs significantly from the oxidation of pure Cu that constantly maintains the Cu_2O/CuO bilayer growth without approaching termination, albeit the overall oxide growth rate slows down with increasing thickness of the oxide (i.e., Wagner's parabolic rate law).

This difference in the oxidation behavior between pure Cu and Cu_3Pt can be attributed to the selective oxidation of Cu in Cu_3Pt. As shown in AP XPS measurements (Figs. 3–5), the selective oxidation of Cu results in the enrichment of Pt underneath the oxide/alloy interface, for which the supply of Cu from deeper atomic layers through the Pt-rich layer to the oxide/alloy interface can be significantly hindered. The XPS-measured Pt enrichment under the oxide/alloy interface is also consistent with the *in situ* electron microscopy observations of the oxidation of Cu-Pt, showing that the Cu_2O island growth results in the significant accumulation of Pt in the alloy adjacent to the Cu_2O/alloy interface [47]. It is also informative to compare the oxidation of $Cu_3Pt(100)$ to that of $Cu_3Au(100)$. Our previous AP XPS measurements showed that the $Cu_3Au(100)$ oxidation under similar conditions results in the constant Cu_2O/CuO bilayer growth [27], which is different from the oxidation of Cu_3Pt but similar to pure Cu. The difference between $Cu_3Pt(100)$ and $Cu_3Au(100)$ can be attributed to the different ways of the selective oxidation of Cu-induced redistribution of Au and Pt due to the different mobilities of Au and Pt in the Cu-Au and Cu-Pt alloys. Because of their stable electronic configurations, both Au and Pt do not go into solution in the Cu oxides. Therefore, the oxidation of $Cu_3Pt(100)$ and $Cu_3Au(100)$ leads to rejection of the noble metals from the oxide/alloy interface to the remaining Cu_3Pt and Cu_3Au alloys, respectively. The activation energies

for bulk diffusion of Pt in Cu and Au in Cu are ∼1.51 eV [58] and ∼1.1 eV [59], respectively. Thus, Pt atoms rejected from the oxide growth during the oxidation of the Cu-Pt alloy tend to remain in the alloy adjacent to the oxide/alloy interface due to the sluggish mobility of Pt atoms, where the enriched Pt layer can hinder the diffusion of Cu from the bulk toward the oxide/alloy interface. By contrast, Au atoms rejected from oxide growth during the oxidation of the Cu-Au alloy can diffuse away from the oxide/alloy interface and spread out in the alloy, thereby allowing for the continued supply of Cu from deeper atomic layers to the oxide/alloy interface to sustain the reaction.

Cu and Cu alloys are often used under the conditions where surface oxidation can significantly affect their performance and functionalities. For instance, Cu and its alloys are widely used as interconnect materials in the fabrication of integrated circuits because of their high electrical and thermal conductivities. However, one major issue is that Cu is vulnerable to oxidation naturally, especially during the electronic packaging assembly process that typically involves harsh environments such as elevated temperature and reactive gases. Unlike aluminum oxide, the Cu oxide layer is not self-protective, and the oxidation of Cu continues. Cu oxidation is considered as a major reliability problem for the development of high-density integrated circuit packaging and lead-free soldering. As discussed above, Cu-Pt shows improved oxidation resistance compared to pure Cu and Cu-Au alloys. The surface oxidation resistance of Cu can be improved by surface alloy such as through plating with Pt, which may find applicability in improving the environmental stability of Cu base alloys. This has been even more desired as dimensions of engineered systems continue to shrink to the nanoscale, where the environmental stability is critical for the performance of nanodevices. Another example is heterogeneous catalysis that uses Cu and Cu alloys as catalysts for a wide variety of catalytic oxidation reactions such as methanol oxidation [60], steaming reforming [61], and the water-gas-shift reactions [62]. For these chemical processes, a critical issue is related to the surface oxidation of Cu that may lead to significant changes to the catalytic performance of Cu-based catalysts [63]. As discussed above, the oxidation of Cu and Cu-Au alloys results in the mixed oxides of Cu_2O and CuO whereas the final product from the oxidation of the Cu-Pt alloy is CuO. Such differences in the oxide formation may be employed to control the oxidation state of the metal atoms and thus modify the reactivity and selectivity of Cu-containing catalysts.

V. CONCLUSION

We have studied the surface composition evolution of $Cu_3Pt(100)$ in response to temperature and atmosphere. Under UHV annealing, Cu segregates at the surface along with the enrichment of Pt in the subsurface region. Heating over the bulk order-disorder transition temperature of Cu_3Pt drives the composition homogenization via inward Pt migration from the subsurface region toward the bulk, whereas the topmost atomic layers remain as pure Cu. Upon switching to the O_2 atmosphere, dissociative chemisorption of oxygen does not change the surface segregation profile from that under the UHV condition until the Cu_2O formation at a higher oxygen pressure, for which the selective oxidation of Cu results in accumulation of more Pt underneath the oxide/alloy interface. A further increase in the oxygen pressure gives rise to the complete reaction pathway of $Cu \rightarrow Cu_2O \rightarrow CuO$, in which CuO grows at the expense of the Cu_2O. The Pt-enriched subsurface hinders the supply of Cu from the bulk toward the oxide/alloy interface, thereby leading to the termination of the surface oxidation after the Cu_2O is completely transformed into CuO. This differs from the oxidation pathway of $Cu \rightarrow Cu_2O \rightarrow Cu_2O/CuO$ for Cu and Cu-Au alloys, in which the Cu_2O/CuO bilayer growth is constantly maintained with the continued oxidation of Cu. These results may have broader practical implications in alloy design for controlling the surface properties of Cu-based alloys such as corrosion resistance and catalytic activities.

ACKNOWLEDGMENTS

This work was supported by the U.S. Department of Energy, Office of Basic Energy Sciences, Division of Materials Sciences and Engineering under Award No. DE-SC0001135. This research used resources of the Center for Functional Nanomaterials, the 23-ID-2 beamline at the National Synchrotron Light Source II, and the Scientific Data and Computing Center, a component of the Computational Science Initiative, at Brookhaven National Laboratory which is supported by the U.S. Department of Energy, Office of Basic Energy Sciences, under Contract No. DE-SC0012704. This work also used the computational resources from the Extreme Science and Engineering Discovery Environment (XSEDE) through Allocation No. TG-DMR110009, which is supported by the National Science Foundation Grant No. OCI-1053575.

[1] A. Bergmann and B. Roldan Cuenya, Operando insights into nanoparticle transformations during catalysis, ACS Catal. **9**, 10020 (2019).

[2] L. Liu and A. Corma, Metal catalysts for heterogeneous catalysis: From single atoms to nanoclusters and nanoparticles, Chem. Rev. **118**, 4981 (2018).

[3] H. Lee, Y. Sohn, and C. K. Rhee, Pt deposits on Bi/Pt NP catalyst for formic acid oxidation: Catalytic enhancement and longer lifetime, Langmuir **36**, 5359 (2020).

[4] A. Sarkar and A. Manthiram, Synthesis of Pt@Cu core−shell nanoparticles by galvanic displacement of Cu by Pt^{4+} ions and their application as electrocatalysts for oxygen reduction reaction in fuel cells, J. Phys. Chem. C **114**, 4725 (2010).

[5] S. Lee, S. Jeong, W. D. Kim, S. Lee, K. Lee, W. K. Bae, J. H. Moon, S. Lee, and D. C. Lee, Low-coordinated surface atoms of CuPt alloy cocatalysts on TiO_2 for enhanced photocatalytic conversion of CO_2, Nanoscale **8**, 10043 (2016).

[6] I. E. L. Stephens, A. S. Bondarenko, F. J. Perez-Alonso, F. Calle-Vallejo, L. Bech, T. P. Johansson, A. K. Jepsen, R. Frydendal, B. P. Knudsen, and J. Rossmeisl, Tuning the activity of Pt (111) for oxygen electroreduction by subsurface alloying, J. Am. Chem. Soc. **133**, 5485 (2011).

[7] A. Wolfbeisser, B. Klötzer, L. Mayr, R. Rameshan, D. Zemlyanov, J. Bernardi, K. Föttinger, and G. Rupprechter, Surface modification processes during methane decomposition on Cu-promoted Ni-ZrO_2 Catalysts, Catal. Sci. Technol. **5**, 967 (2015).

[8] M. Salmeron and R. Schlögl, Ambient pressure photoelectron spectroscopy: A new tool for surface science and nanotechnology, Surf. Sci. Rep. **63**, 169 (2008).

[9] B. Eren, R. S. Weatherup, N. Liakakos, G. A. Somorjai, and M. Salmeron, Dissociative carbon dioxide adsorption and morphological changes on Cu (100) and Cu (111) at ambient pressures, J. Am. Chem. Soc. **138**, 8207 (2016).

[10] I. Orozco, E. Huang, M. Mahapatra, R. Shi, J. Kang, S. Nemsak, S. D. Senanayake, P. Liu, and J. A. Rodriguez, *In situ* studies of methanol decomposition over Cu (111) and Cu_2O/Cu (111): Effects of reactant pressure, surface morphology, and hot spots of active sites, J. Phys. Chem. C **125**, 558 (2020).

[11] A. M. Motin, T. Haunold, A. V. Bukhtiyarov, A. Bera, C. Rameshan, and G. Rupprechter, Surface science approach to Pt/carbon model catalysts: XPS, STM and microreactor studies, Appl. Surf. Sci. **440**, 680 (2018).

[12] S. L. Bergman, J. Granestrand, Y. Tang, R. S. París, M. Nilsson, F. F. Tao, C. Tang, S. J. Pennycook, L. J. Pettersson, and S. L. Bernasek, *In-situ* characterization by near-ambient pressure XPS of the catalytically active phase of Pt/Al_2O_3 during NO and CO oxidation, Appl. Catal., B **220**, 506 (2018).

[13] Y. Yu, Y. E. Koh, H. Lim, B. Jeong, K. Isegawa, D. Kim, K. Ueda, H. Kondoh, K. Mase, and E. J. Crumlin, Chemical states of surface oxygen during CO oxidation on Pt (110) surface revealed by ambient pressure XPS, J. Phys.: Condens. Matter **29**, 464001 (2017).

[14] B. Eren, C. Heine, H. Bluhm, G. A. Somorjai, and M. Salmeron, Catalyst chemical state during CO oxidation reaction on Cu (111) studied with ambient-pressure x-ray photoelectron spectroscopy and near edge x-ray adsorption fine structure spectroscopy, J. Am. Chem. Soc. **137**, 11186 (2015).

[15] T. Abe, B. Sundman, and H. Onodera, Thermodynamic assessment of the Cu-Pt system, J. Phase Equilib. Diffus. **27**, 5 (2006).

[16] K. Mitsui, M. Takahashi, and T. Takezawa, Effect of ternary addition on the formation of Cu_3Pt and CuPt order phases in the Cu-Pt system, Philos. Mag. Lett. **77**, 49 (1998).

[17] X. Guo, Y. Zhang, C. Deng, X. Li, Y. Xue, Y.-M. Yan, and K. Sun, Composition dependent activity of Cu-Pt nanocrystals for electrochemical reduction of CO_2, Chem. Commun. **51**, 1345 (2015).

[18] N. Schumacher, K. Andersson, L. C. Grabow, M. Mavrikakis, J. Nerlov, and I. Chorkendorff, Interaction of carbon dioxide with Cu overlayers on Pt (111), Surf. Sci. **602**, 702 (2008).

[19] J. Knudsen, A. U. Nilekar, R. T. Vang, J. Schnadt, E. L. Kunkes, J. A. Dumesic, M. Mavrikakis, and F. Besenbacher, A Cu/Pt near-surface alloy for water−gas shift catalysis, J. Am. Chem. Soc. **129**, 6485 (2007).

[20] K. J. Andersson, F. Calle-Vallejo, J. Rossmeisl, and I. Chorkendorff, Adsorption-driven surface segregation of the less reactive alloy component, J. Am. Chem. Soc. **131**, 2404 (2009).

[21] J. P. Simonovis, A. Hunt, and I. Waluyo, *In situ* ambient pressure XPS study of Pt/Cu (111) single-atom alloy in catalytically relevant reaction conditions, J. Phys. D: Appl. Phys. **54**, 194004 (2021).

[22] Y. G. Shen, D. J. O'Connor, K. Wandelt, and R. J. MacDonald, Studies of surface composition and structure of Cu_3Pt (111) by low energy alkali ion scattering, Surf. Sci. **328**, 21 (1995).

[23] Y. G. Shen, D. J. O'Connor, and K. Wandelt, The surface composition, structure and oxygen-induced (2× 1) reconstruction of Cu_3Pt (110), Surf. Sci. **410**, 1 (1998).

[24] Y. G. Shen, D. J. O'Connor, and K. Wandelt, Composition and structure of Cu_3Pt (001): A (1× 1) Cu termination with c (2× 2) underlayer ordering, Surf. Sci. **406**, 23 (1998).

[25] Y. Gauthier, A. Senhaji, B. Legrand, G. Tréglia, C. Becker, and K. Wandelt, An unusual composition profile: A LEED–TBIM study of $Pt_{25}Cu_{75}$ (111), Surf. Sci. **527**, 71 (2003).

[26] R. Yang, P. Strasser, and M. F. Toney, Dealloying of Cu_3Pt (111) studied by surface x-ray scattering, J. Phys. Chem. C **115**, 9074 (2011).

[27] C. Li, Q. Liu, J. A. Boscoboinik, and G. Zhou, Tuning the surface composition of Cu_3Au binary alloy, Phys. Chem. Chem. Phys. **22**, 3379 (2020).

[28] C. Li, P. Zhang, J. Wang, J. A. Boscoboinik, and G. Zhou, Tuning the deoxygenation of bulk-dissolved oxygen in copper, J. Phys. Chem. C **122**, 8254 (2018).

[29] J. Wang, C. Li, Y. Zhu, J. A. Boscoboinik, and G. Zhou, Insight into the phase transformation pathways of copper oxidation: From oxygen chemisorption on the clean surface to multilayer bulk oxide growth, J. Phys. Chem. C **122**, 26519 (2018).

[30] J. Wang, D. Lu, C. Li, Y. Zhu, J. A. Boscoboinik, and G. Zhou, Measuring charge transfer between adsorbate and metal surfaces, J. Phys. Chem. Lett. **11**, 6827 (2020).

[31] G. Kresse and J. Furthmüller, Efficiency of *ab-initio* total energy calculations for metals and semiconductors using a plane-wave basis set, Comput. Mater. Sci. **6**, 15 (1996).

[32] G. Kresse and J. Furthmüller, Efficient iterative schemes for *ab initio* total-energy calculations using a plane-wave basis set, Phys. Rev. B **54**, 11169 (1996).

[33] G. Kresse and J. Hafner, *Ab initio* molecular dynamics for liquid metals, Phys. Rev. B **47**, 558 (1993).

[34] G. Kresse and J. Hafner, *Ab Initio* molecular-dynamics simulation of the liquid-metalamorphous- semiconductor transition in germanium, Phys. Rev. B **49**, 14251 (1994).

[35] J. P. Perdew, J. A. Chevary, S. H. Vosko, K. A. Jackson, M. R. Pederson, D. J. Singh, and C. Fiolhais, Atoms, molecules, solids, and surfaces: Applications of the generalized gradient approximation for exchange and correlation, Phys. Rev. B **46**, 6671 (1992).

[36] G. Kresse and D. Joubert, From ultrasoft pseudopotentials to the projector augmented-wave method, Phys. Rev. B **59**, 1758 (1999).

[37] C. J. Zhang, R. J. Baxter, P. Hu, A. Alavi, and M.-H. Lee, A density functional theory study of carbon monoxide oxidation on the Cu_3Pt(111) alloy surface: Comparison with the reactions on Pt(111) and Cu(111), J. Chem. Phys. **115**, 5272 (2001).

[38] B. R. Strohmeier, An ESCA method for determining the oxide thickness on aluminum alloys, Surf. Interface Anal. **15**, 51 (1990).

[39] M. P. Seah and W. A. Dench, Quantitative electron spectroscopy of surfaces: A standard data base for electron inelastic mean free paths in solids, Surf. Interface Anal. **1**, 2 (1979).

[40] I. Khalakhan, M. Vorokhta, X. Xie, L. Piliai, and I. Matolínová, On the interpretation of x-ray photoelectron spectra of Pt-Cu bimetallic alloys, J. Electron Spectrosc. Relat. Phenom. **246**, 147027 (2021).

[41] N. T. Barrett, R. Belkhou, J. Thiele, and C. Guillot, A core-level photoemission spectroscopy study of the formation of surface alloy Cu/Pt(111): Comparison with Pt/Cu(111), Surf. Sci. **331–333**, 776 (1995).

[42] Y.-S. Lee, K.-Y. Lim, Y.-D. Chung, C.-N. Whang, and Y. Jeon, XPS core-level shifts and XANES studies of Cu-Pt and Co–Pt alloys, Surf. Interface Anal. **30**, 475 (2000).

[43] G.-W. Zhou, L. Wang, R. C. Birtcher, P. M. Baldo, J. E. Pearson, J. C. Yang, and J. A. Eastman, Cu_2O Island Shape Transition During Cu-Au Alloy Oxidation, Phys. Rev. Lett. **96**, 226108 (2006).

[44] G. Zhou, L. Luo, L. Li, J. Ciston, E. A. Stach, W. A. Saidi, and J. C. Yang, *In Situ* atomic-scale visualization of oxide islanding during oxidation of Cu surfaces, Chem. Commun. **49**, 10862 (2013).

[45] G. W. Zhou, TEM investigation of interfaces during cuprous island growth, Acta Mater. **57**, 4432 (2009).

[46] G. Zhou and J. C. Yang, Initial oxidation kinetics of Cu(100), (110), and (111) thin films investigated by *in situ* ultra-high-vacuum transmission electron microscopy, J. Mater. Res. **20**, 1684 (2005).

[47] L. Luo, Y. Kang, J. C. Yang, D. Su, E. A. Stach, and G. Zhou, Comparative study of the alloying effect on the initial oxidation of Cu-Au(100) and Cu-Pt(100), Appl. Phys. Lett. **104**, 121601 (2014).

[48] N. S. McIntyre and M. G. Cook, X-ray photoelectron studies on some oxides and hydroxides of cobalt, nickel, and copper, Anal. Chem. **47**, 2208 (1975).

[49] U. Schneider, G. R. Castro, and K. Wandelt, Adsorption on ordered $Cu_3Pt(111)$: Site selectivity, Surf. Sci. **287–288**, 146 (1993).

[50] F. R. Boer, R. Boom, W. C. M. Mattens, A. R. Miedema, and A. K. Niessen, *Cohesion in Metals: Transition Metal Alloys, Vol. 1* (North Holland, Amsterdam, 1988).

[51] X. Duan, O. Warschkow, A. Soon, B. Delley, and C. Stampfl, Density functional study of oxygen on Cu(100) and Cu(110) surfaces, Phys. Rev. B **81**, 075430 (2010).

[52] L. Li, X. Mi, Y. Shi, and G. Zhou, Precursor to the Onset of the Bulk Oxidation of Cu(100), Phys. Rev. Lett. **108**, 176101 (2012).

[53] K. H. Schulz and D. F. Cox, Photoemission and low-energy-electron-diffraction study of clean and oxygen-dosed Cu_2O (111) and (100) surfaces, Phys. Rev. B **43**, 1610 (1991).

[54] L. Yuan and G. Zhou, Enhanced CuO nanowire formation by thermal oxidation of roughened copper, J. Electrochem. Soc. **159**, C205 (2012).

[55] J. Rebane, N. Yakovlev, D. Chicherin, L. Leonyuk, and V. Yakunin, An experimental study of copper self-diffusion in CuO, $Y_2Cu_2O_5$ and $YBa_2Cu_3O_{7-x}$ by secondary neutral mass spectrometry, J. Mater. Chem. **7**, 2085 (1997).

[56] N. L. Peterson and C. L. Wiley, Diffusion and point defects in Cu_2O, J. Phys. Chem. Solids **45**, 281 (1984).

[57] R. Mema, L. Yuan, Q. Du, Y. Wang, and G. Zhou, Effect of surface stresses on CuO nanowire growth in the thermal oxidation of copper, Chem. Phys. Lett. **512**, 87 (2011).

[58] A. N. Aleshin, V. K. Egorov, B. S. Bokstein, and P. V. Kurkin, Study of Pt diffusion in thin copper films under two kinetic regimes, J. Appl. Phys. **77**, 6239 (1995).

[59] A. N. Aleshin, B. S. Bokstein, V. K. Egorov, and P. V. Kurkin, Grain boundary and bulk diffusion in Au-Cu thin Films, in *Defect and Diffusion Forum*, Vol. 95, edited by M. Koiwa, K. Hirano, H. Nakajima, and T. Okada (Trans Tech Publications, Stäfa-Zürich, Switzerland, 1993), pp. 457–462.

[60] S. M. Francis, F. M. Leibsle, S. Haq, N. Xiang, and M. Bowker, Methanol oxidation on Cu(110), Surf. Sci. **315**, 284 (1994).

[61] X.-K. Gu and W.-X. Li, First-principles study on the origin of the different selectivities for methanol steam reforming on Cu(111) and Pd(111), J. Phys. Chem. C **114**, 21539 (2010).

[62] J. A. Rodriguez, P. Liu, X. Wang, W. Wen, J. Hanson, J. Hrbek, M. Pérez, and J. Evans, Water-gas shift activity of Cu surfaces and Cu nanoparticles supported on metal oxides, Catal. Today **143**, 45 (2009).

[63] J. Li and G. Zhou, Density functional theory study of O–H and C–H bond scission of methanol catalyzed by a chemisorbed oxygen layer on Cu(111), Surf. Sci. **646**, 288 (2016).